Sustainable Materials and Technologies 40 (2024) e00933

Contents lists available at ScienceDirect

Sustainable Materials and Technologies

journal homepage: www.elsevier.com/locate/susmat

# From ashes to porous hierarchical nanocarbon electrode: Upcycling secondary waste materials through self-catalytic chemical vapour deposition

Maciej J. Głowacki [a], Katarzyna Karpienko [a], Maciej S. Wróbel [a], Karol Szczodrowski [b], Chiara Giosuè [c], Gianni Barucca [c], Maria Letizia Ruello [c], Robert Bogdanowicz [a], Mattia Pierpaoli [a,*]

[a] Faculty of Electronics, Telecommunications and Informatics, Gdańsk University of Technology, Gabriela Narutowicza 11/12, 80-233 Gdańsk, Poland
[b] Faculty of Mathematics, Physics and Informatics, University of Gdańsk, Wita Stwosza 57, 80-308 Gdańsk, Poland
[c] Department of Science and Engineering of Matter, Environment and Urban Planning (SIMAU), Università Politecnica delle Marche, INSTM Research Unit, Via Brecce Bianche 12, 60131 Ancona, Italy

ARTICLE INFO

*Keywords:*
Fly ash
Carbon nanomaterials
CVD
Electrochemical oxidation
Circular economy

ABSTRACT

Metal and metal oxide particles are abundant in various ash-based wastes. Utilising these as catalyst sources for the fabrication of carbon nanomaterials could present a valuable approach to reduce our reliance on non-renewable and costly catalyst sources, thereby facilitating large-scale nanomaterial production. In this context, secondary waste materials (SWMs) are by-products resulting from the (complete or partial) combustion of carbon-rich sources or other industrial processes and their disposal poses a serious environmental problem. In this study, we demonstrate a novel strategy to upcycle SWMs as catalysts, as received, for the growth of carbon nanoarchitectured electrodes through microwave plasma-enhanced chemical vapour deposition (MPECVD), without the need for functionalisation. Firstly, 10 SWMs were selected to fabricate porous hierarchical nanocarbon (PHN) electrodes by phase-inversion and subsequent catalytic MPECVD growth. Secondly, distinct growth conditions, both in the presence and absence of $CH_4$ as an external carbon source were applied, resulting in conductive electrodes, on which acetaminophen oxidation was performed. Results show that not all SWMs, despite originating from similar processes, work as a catalyst. In particular, principal component analysis suggests the presence of calcium oxosilicate and calcium-magnesium-iron carbonate as potential catalysts, which are present in two SWMs. Contrary to what might be expected, the occurrence of metals, such as Fe, Ni, is not a sufficient factor for the catalytic growth of carbon nanostructures. Interestingly, water vapour adsorption isotherms suggest the formation of different porous networks according to the specific SWMs. Finally, the development of waste-derived catalysts fosters the concept of upcycling, converting waste into higher-value products, thus closing the loop on resource utilisation and minimising waste generation.

## 1. Introduction

The use of waste materials as catalysts has emerged as an important research frontier in the field of chemical engineering and represents a crucial step towards sustainable and environmentally conscious practices [1]. The conventional reliance on costly and often scarce traditional catalysts has spurred the need to explore alternative, greener ways of catalysing chemical reactions. Industrial waste materials represent a promising reservoir of resources that can be converted into valuable catalysts, offering a dual solution to the pressing challenges of waste management and sustainable and cleaner chemical production. Various low-cost by-products from agricultural, household, and industrial sectors are being repurposed, not only in wastewater treatment [2], but also in transforming plastic waste into carbon-based nanomaterials [3]. This innovation, however, is often challenged by the need for more rigorous characterisation of the resulting carbon material [4].

Over the past twenty years, catalytic chemical vapour deposition (CCVD) has significantly expanded, especially as a preferred method for

* Corresponding author.
*E-mail address:* mattia.pierpaoli@pg.edu.pl (M. Pierpaoli).

https://doi.org/10.1016/j.susmat.2024.e00933
Received 13 November 2023; Received in revised form 25 March 2024; Accepted 10 April 2024
Available online 16 April 2024

creating carbon nanotubes (CNTs) and nanofibres, due to its superior control and scalability [5]. Traditionally, CCVD relies on nanoparticles primarily made from transition metals like iron, nickel, or cobalt [6]. These particles are often anchored on zeolites or porous substrates [7]. However, recent studies have identified a range of efficient catalysts, including hydrotalcite-related compounds [8] and calcium titanate [9]. The application of gold ore tailings in decorating $TiO_2$ substrates for catalytic growth [10], and the use of Fe-rich fly ashes, sometimes enhanced with nickel, for supporting CNTs growth [11], exemplify material substitution in action. These practices also underscore the potential of emerging materials in developing efficient sustainable energy and environmental devices. The role of fly ashes, particularly their varied origins and complex matrices, in influencing the CCVD process, however, remains underexplored [12]. Isolated Fe-rich spherical particles from fly ashes have been utilized as support for cementite core@-graphite shell composites with exceptional microwave adsorption properties [13]. Although some authors attribute the presence of iron (as oxide) in fly ashes to the growth of carbon nanofibres (CNFs), there is still a gap in research when it comes to studying various fly ashes originating from diverse industrial processes. Additionally, fly ashes are complex matrices with other constituents that could influence the CCVD process. From a systematic comparison of fly ash used as support and catalyst in CCVD, reported in Table S1, it is possible to observe that most of the studies considered lack practical applications, while we support the use of these as catalysts and fillers for the synthesis of critical raw materials-free electrodes for the oxidation of water pollutants [14]. Indeed, using fly ashes and other secondary waste materials as a substrate and catalyst for the growth of carbon nanomaterials offers several benefits, among which there are: cost-effectiveness, waste-utilisation and structural diversity. Cu has been reported as a catalyst for helical carbon nanofibres' growth, with catalyst particle size and shape significantly affecting the growth mode [15]. Furthermore, different geometrical structures of CNTs have been observed based on the degree of polymerisation of PVA during catalytic decomposition [16]. While fly ashes from coal combustion (CFA) are extensively explored as catalysts, nanoparticles from solid waste fly ash and zeolite derived from bottom ash have also been used for CCVD [17], or zeolite have been derived from bottom ash, decorated with CNTs to enable $CO_2$ capture [18]. The impact of carbon content in various allotropic forms on the CCVD process as a catalyst itself remains an open question. Char is a pyrolysis by-product, and it is characterised by a high porosity and may be regarded as a renewable and low-cost source of carbon materials. For this reason, it has been investigated as substrate for the growth of CNTs, with the addition of nickel as a catalyst, finding that the presence of Ni was critical for the formation of CNTs and that CNTs did not form under conventional fixed-bed heating conditions and that microwave irradiation played a key role in the synthesis of CNTs [19]. Similarly, Li et al. sprayed a $Ni(NO_3)_2$ solution onto CFA-based membrane to catalyse the growth of CNTs using waste polypropylene as carbon source, in the field of solar membrane distillation. Up to the authors' knowledge, waste foundry sand (WFS), a major pollutant generated from metal casting foundries, and bottom ashes originated from the incineration of sewage sludge, both classified as hazardous materials, have never been investigated as catalytic substrates for the CVD growth of carbon nanostructures, despite their rich composition in metal impurities. To summarise, various undoped carbon nanomaterial (CNM) morphologies were observed when FA were subjected to pyrolysis in the presence of an organic precursor. However, the synthesis of hetero-codoped CNMs over fly ashes has not been reported yet. While CNT electrochemical activity can be enhanced with N-doping, due to the net positive charge resulting from the carbon atoms [20], B-doping results in a faster kinetic transfer rate [21], or the formation of specific chemical bonds [22]. Moreover, $B_2H_6$ as B-precursor has the role to control the re-nucleation and twinning surface process of the CVD-grown graphene stacks [23].

Our study presents a novel approach in developing functional porous hierarchical nanocarbons (PHN) electrodes by upcycling secondary waste materials through the CCVD method. We demonstrate the growth of nanostructured carbon on these materials without external catalysts and highlight the superior electrochemical properties of the resulting composites. Employing SWMs in the fibre results in enhancing its volumetric mechanical and electrical properties and provding a catalyst mixture for growing CNMs during microwave plasma-enhanced chemical vapour deposition (MPECVD). In our study, we pioneer the comparison of various secondary waste materials (SWMs) as potential fillers and catalysts in the synthesis of electrochemically active porous hierarchical nanocarbons (PHN), specifically targeting the oxidation of acetaminophen. While catalytic chemical vapour deposition (CCVD) has predominantly been applied to fly ashes, the precise factors contributing to its effectiveness—whether the specific form of carbon used or the presence of certain metallic impurities acting as catalysts—remain unclear. To address this gap, we have meticulously selected a diverse array of 10 different SWMs, supplemented by 3 alternative fillers, to represent a broad spectrum of industrial by-products. This selection enables a comprehensive exploration of how different SWMs, when integrated into microfibrous matrices, influence the final properties of the CNM composites. Our investigation encompasses the entire process, from the initial design of nanomaterial dispersions to the detailed morphological and electrochemical characterisations of the CNM composites. Emphasising the fine-tuning of synthesis parameters, our approach aims to elucidate the multifaceted interactions within these complex systems, thereby advancing our understanding of material science in sustainable energy and environmental applications.

## 2. Materials and methods

### 2.1. Materials

Polyacrylonitrile (PAN, >98%) was purchased from Aldrich. Dimethylformamide (DMF, pure p.a.), potassium ferricyanide ($K_3[Fe(CN)_6]$ and $K_4[Fe(CN)_6]\bullet 3H_2O$) were acquired from POCH (Poland). Phosphate buffer (PB 0.1 M) solution was obtained by mixing 8.7331 g of $K_2HPO_4$ and 125 μL of 85% $H_3PO_4$ in a 500 mL volumetric flask with deionized water. The different types of SWMs are shortly described in Table 1, where also the relevant information on the source and the type of treatment is reported. SWMs were kindly donated by their respective producers. Alternative fillers (AFs) were used as representative materials, characterised by a known chemical composition and properties.

**Table 1**
List of SWMs and technical fillers employed in the current study.

| | Sample ID | Sample type | Type of combustion |
|---|---|---|---|
| SWM | C-IT1 | Char from pure biomass source | Limited presence of oxygen (gasification) |
| | C-IT2 | Char from pure biomass source | Limited presence of oxygen (gasification) |
| | C-SR | Char from pure biomass source with high presence of silicates | Limited presence of oxygen (gasification) |
| | BC-UK | Char from pure biomass source | Limited presence of oxygen (gasification) |
| | CFA | Fly ash from coal thermo-valorization | Oxidising atmosphere (thermal combustion) |
| | BFA-USA | Fly ash from biomass source | Oxidising atmosphere (thermal combustion) |
| | BFA-FI1 | Fly ash from biomass source | Oxidising atmosphere (thermal combustion) |
| | BFA-IT3 | Fly ash from biomass source | Oxidising atmosphere (thermal combustion) |
| | SSA-PL1 | Bottom ash from sewage sludge | Oxidising atmosphere (thermal combustion) |
| | FS | Used foundry sand | Oxidising atmosphere (up to 1400 °C) |
| AF | Z | Zeolite | – |
| | G | Graphite | – |
| | AC | Activated carbon | – |

Zeolite (Z), a silicate-based material, mechanically-exfoliated graphite (G) and a commercially-available activated carbon (AC) were chosen as AFs due to their absence and predominant presence of allotropic carbons.

### 2.2. Electrode fabrication

Electrode fabrication and characterisation procedure is schematically displayed in Fig. 1.

To prepare the carbon nanocomposite nanostructured electrodes a 10%*w*/w PAN/DMF stock solution was first prepared and stirred for 24 h. Then, a predetermined amount of SWM or AF was added to the polymer blend to obtain a 25%w dispersion. The resulting solution was then wet-spun using a laboratory fabricated apparatus [24] to obtain a continuous fibre. The fibre was then formed into a flat cylinder with a diameter of 16 mm and a height of 3 mm. The resulting pellet was then stabilised in a furnace at 240 °C for 3 h at a heating rate of 1 °C/min. Finally, carbonisation and CVD growth were performed in a single step by MPECVD. For each composite electrode, two different CVD processes were carried out in which the gas composition was varied to compare the effect of pure $H_2$ plasma with that of an $H_2$, $CH_4$-rich atmosphere in the presence of $B_2H_6$ as dopant [22].

### 2.3. Porous hierarchical nanocarbons characterisation

The morphology and size distributions of the SWMs were characterised by SEM, DLS, while their chemical composition was assessed by EDX, XRD, Raman spectroscopy and by inductively coupled plasma optical emission spectroscopy (ICP-OES). A Phenom XL Scanning Electron Microscope (SEM, operating in low vacuum mode with a 15 kV beam acceleration voltage) was used to characterise the raw SWMs, while for the electrodes a FEI Quanta FEG 250 (15 kV, ETD) was used. To further investigate the MPECVD carbon coatings, transmission electron microscopy (TEM) analysis was performed on selected electrodes by using a Philips CM200 microscope operating at 200 kV and equipped with a LaB6 filament. For TEM observations, a portion of the electrode surface was gently scratched with a scalpel blade. The powder produced was dispersed in ethanol and sonicated for 1 min. Finally, a drop of the suspension was put over a commercial carbon-holed TEM grid and kept in air until complete ethanol evaporation. The particle size distribution of the SWMs was assessed by SEM image analysis and dynamic light scattering (DLS). SWMs were dispersed in deionised water, placed in disposable polystyrene cuvettes and analysed using a DLS Zetasizer Nano ZS particle analyser (Malvern Panalytical, UK) equipped with a 632.8 nm laser. Measurements were made at 25 °C using backscatter analysis (light collected at 173°). Each sample was measured 3 times.

The qualitative analysis of the phase composition of the samples was carried out by X-ray diffraction (XRD) using BRUKER D2PHASER equipment with Cu Kα radiation (lambda = 1.54 Å), operating at 30 kV and 10 mA. The XRD patterns were collected using a scan step of 0.02° and a count time of 0.4 s per step. Phase analysis was carried out using DIFFRAC.EVA V4.1 evaluating an application from BRUKER and the ICDD PDF-4 database (release 2021). Principal component analysis (PCA) was performed on the XRD dataset using R statistical environment. Raman scattering was measured using a commercial Raman microscope (LabRam Aramis, Horiba) with excitation by a 632.8 nm HeNe laser with up to 20 mW optical power at the sample. A TE-cooled to −20 °C CCD detector was used with an integration time of 5 s (20 averages); the diffraction grating had 300 lines per mm; the spectral resolution was approximately 2 $cm^{-1}$ in the range 200–3500 $cm^{-1}$; a magnification of ×10 or ×50 was used depending on the sample. Multiple spectra were acquired for each sample, singly in the case of SWM and for both surfaces in the case of the fibrous composites. The baseline was subtracted using the alternating least square smoothing (ALSS) algorithm and the data were normalised and fitted. In order to estimate the incorporation effect of SWMs into the polymer matrix, water vapour isotherms were performed. Solid samples (both SWM powders and electrodes) were first dried in a vacuum oven (105 °C, −60 kPa) for 48 h, weighed and placed in desiccators with a known relative humidity (RH) and continuously monitored by an electronic hygrometer (Table S2). Sigmoidal-shaped isotherm includes type IV and VI isotherms, and these are usually linked to the capillary condensation occurring in micropores. The mathematical model employed to fit the experimental data has been originally presented by Klotz for the binding of organic ions by proteins [25] and adapted for water vapour adsorption on different carbon-based adsorbents [26]. The Klotz isotherm represents a unified concept where all interactions, which are possible between the water and the surface and in between the water molecules itself, are comprised, and it is preferable to the Do-Do model due to the presence of 3 fitting parameters instead of 5, even if it may exhibit strong deviation at high partial pressure [26].

$$\theta = \frac{Cq[1-(1+m)q^m + mq^{m+1}]}{(1-q)[1+(C-1)q - Cq^{m+1}]} \quad (1)$$

In this context, the degree of coverage ($\theta$) is given by “m”, the maximum association number, “q”, determined by the equation q = Kx, where “K” is related to the capillary condensation and “x” is the partial pressure in the bulk phase and C is exponentially related to the energy of monolayer adsorption [27].

The synthesized SWM-containing composites were used as the working electrode. A platinum wire and an Ag/AgCl/3 M KCl electrode were used as auxiliary and reference electrodes, respectively. The

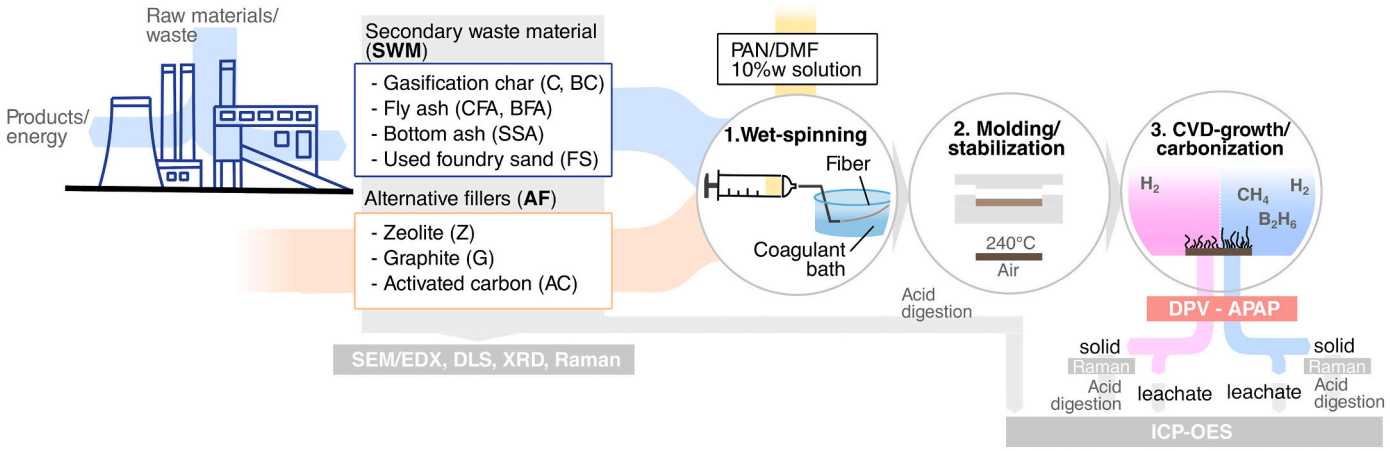


**Fig. 1.** Schematic representation of the hybrid electrode synthesis and characterisation.

electrochemical response was recorded by differential pulse voltammetry (DPV) in 1.5 mL of 0.1 M PB (pH 7.0) containing acetaminophen (APAP) in the 1–100 μM range. After characterisation and each DPV procedure, the liquid sample was collected for further analysis by ICP-OES. To 10 mL of the collected liquid, 1 mL of concentrated $HNO_3$ and 3 mL of concentrated HCl (both trace metal grade acid for ICP-OES (Optical Emission Spectrometer Optima 8300 PerkinElmer) were added in a beaker covered with a watch glass and heated to just below boiling. After cooling to room temperature, the sample was transferred to a 25 mL volumetric flask, the beaker was rinsed and made up to volume with ultrapure water. A similar procedure was followed for the hotplate digestion of the solid sample electrode to obtain a mass balance. Briefly, the dried electrode was ground, weighed and digested on an electric hotplate first with $HClO_4$ and then with aqua regia ($HCl:HNO_3 = 3:1$).

## 3. Results

### 3.1. SWM filler/catalyst characterisation

The large heterogeneity of the raw SWM powders can be observed from the SEM images shown in Fig. 2. All chars are characterised by similar particle shapes, while BFA_FI1 and CFA show a similar composition of both irregular and spherical particles. In particular, it is possible to observe both cenospheres and ferrospheres, typically composed of crystallised Fe-bearing phases dispersed in the aluminosilicate glass matrix [13,28]. FS exhibits the widest particle size distribution, ranging from hundreds of nanometres to hundreds of microns.

The analysis of particle size distributions by DLS is limited by the upper detection limit of the systems, which does not exceed 10 μm (Fig. S1). In SEM images, particle size distributions can be derived from high resolution images by digital analysis. SEM measurements are local in nature and the images obtained show topographies of only selected micro-areas of the analysed materials. Here, both DLS and SEM techniques have been used to provide the most accurate data on the size distributions of particles in SWMs. While DLS was used to investigate particle sizes in aqueous suspensions of SWMs in the range 0.3 nm - 10 μm, SEM images were utilised to estimate information on particle shapes and size distributions above the upper limit. Particle size distributions obtained from DLS measurements were fitted with Gaussian peaks. The maxima and full width at half maximum (FWHMs) of the peaks are summarised in Fig. 3a.

The most abundant elements in SWMs and AFs, detected by EDX analysis, are reported in Table 2. It is worth to point out the large difference in elemental compositions. In particular, different FAs are characterised by a low (average 3.8%, SD 3.4%) C content while char samples by a higher content and wider variability (average 42.1%, SD 16.7%). For both FS and SSA samples, the C content is below 2%. Other predominant elements resulting from EDX analysis are Si, Ca, Fe.

The XRD patterns of the series of samples are shown in Fig. 3b. In Z sample, only orthorhombic $SiO_2$ (PDF 00–043-0784) is distinguishable from the XRD diffractogram, while in FS only hexagonal $SiO_2$ is present as quartz (PDF 00–046-1045), as expected from zeolites and foundry sands. In the case of the AC sample, the well resolved XRD signals can be attributed to the hexagonal $SiO_2$ (PDF 00–046-1045). However, the differences in intensity between the PDF markers and the measured XRD signals suggest that the silica is not well crystallised in quartz form. Other types of $SiO_2$ such as tetragonal (PDF 01–077-8638) and rhombohedral (PDF 04–015-9821) can also be distinguished in the XRD pattern. The main crystallised minerals in SSA-PL1 are quartz (PDF 00–046-1045), calcium aluminium phosphate (PDF 00–048-1192), iron and titanium iron oxides (PDF 04–006-6579, PDF 04–009-5898), which are typical for incinerated sewage sludge samples [29]. The XRD pattern

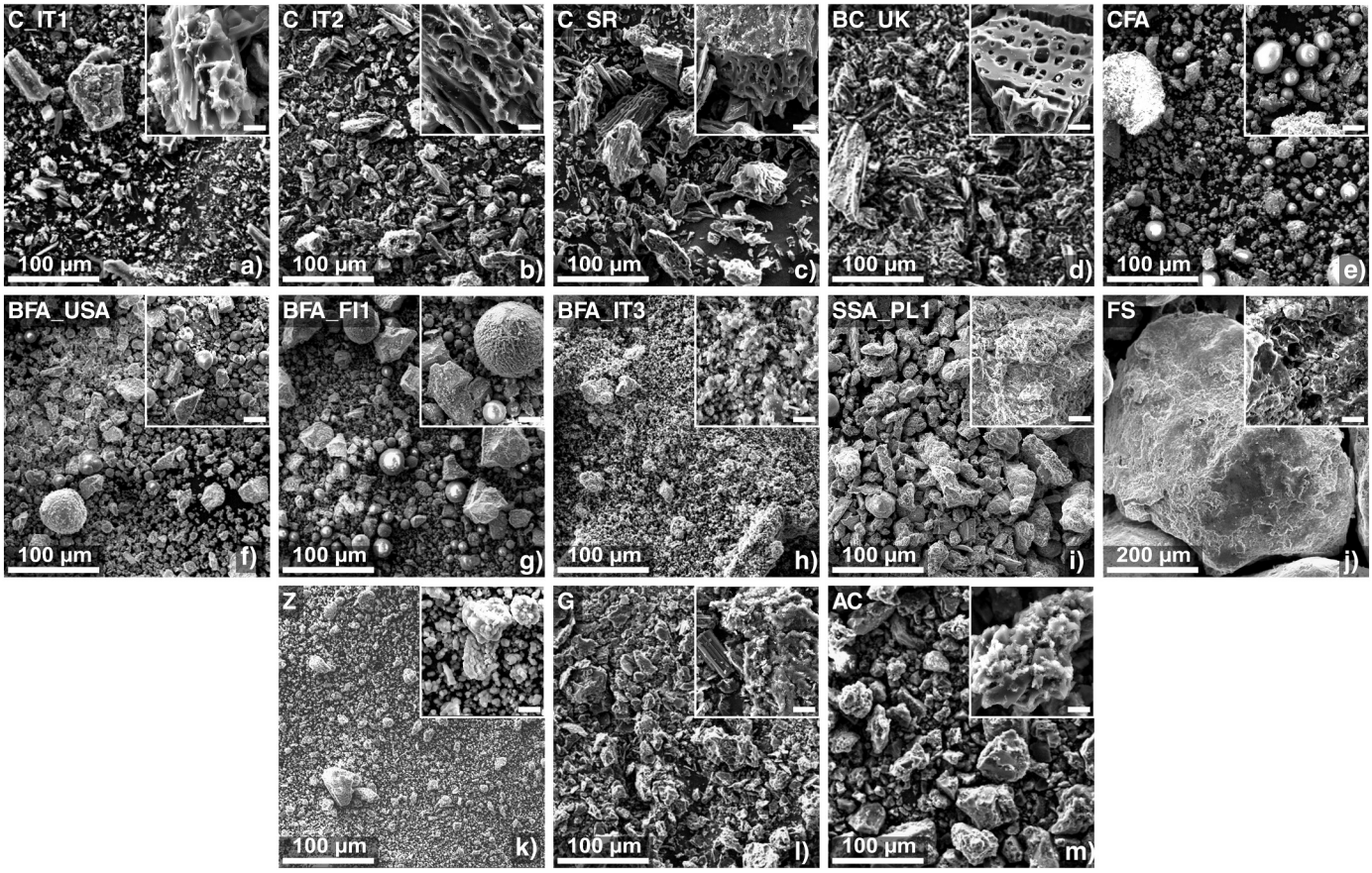


**Fig. 2.** (a-m) SEM of raw SWMs. Inserts are magnification of the SWM, with scale bar equal to 10 μm.

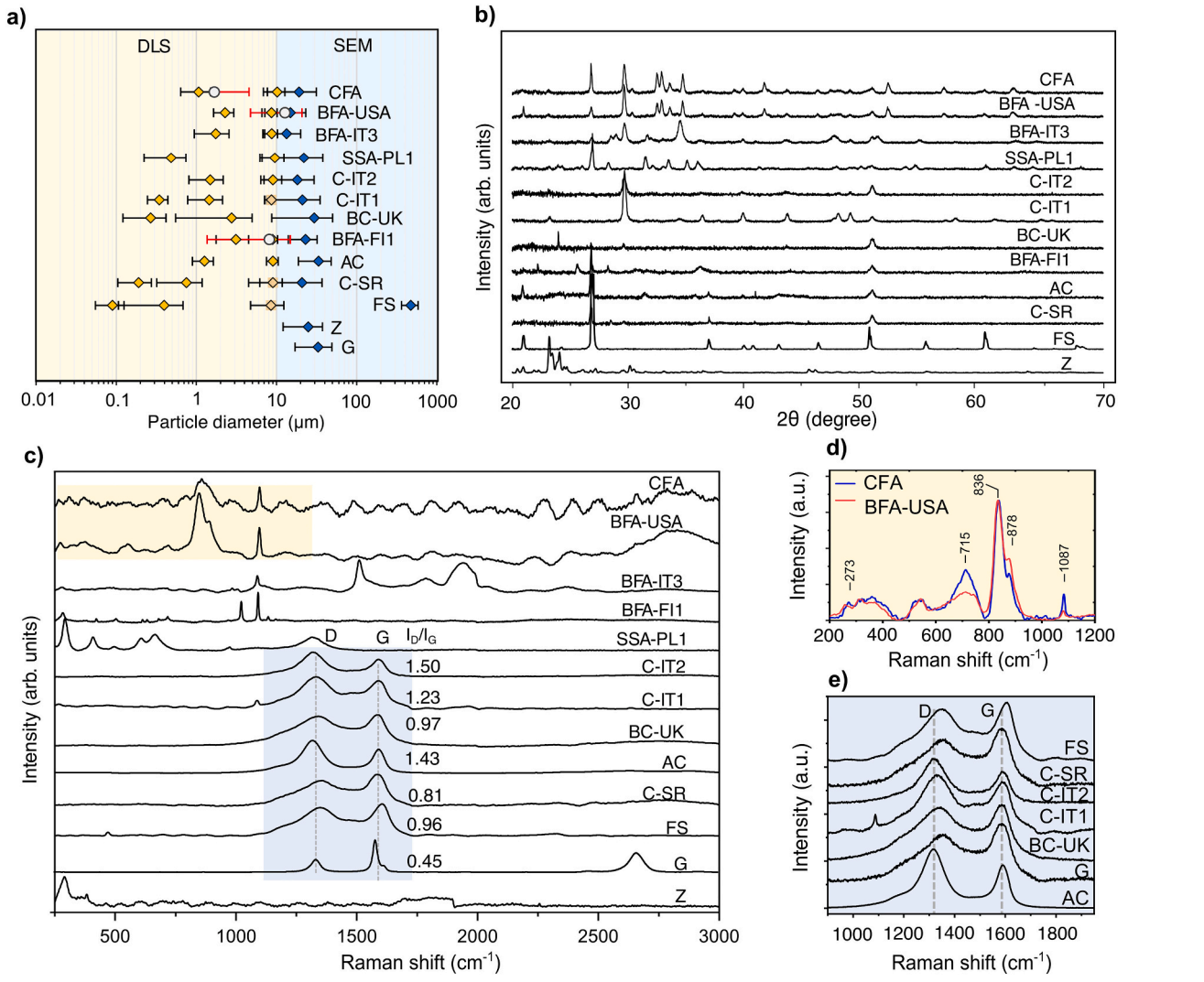


**Fig. 3.** (a) Diameter distribution of the larger particles, estimated by analysis of the SEM images (in blue), and distribution of the submicronic particles, estimated by DLS (in yellow). Bullets are relative to the presence of spherical particles. (b) XRD diffractograms and (c) Raman spectra for all the SWM and magnifications of (d) BFA-USA, CFA, and (e) C-rich fillers (BC-UK, C-IT1, C-IT2, C-SR, FS, AC, and G).

**Table 2**
List of the most abundant elements detected by EDX. Values are expressed as at.% and are the averaged results of EDX analysis in 3 spots.

| Sample | O | C | Si | Na | N | Mg | Ca | K | S | P | Cl | Fe | Al |
|---|---|---|---|---|---|---|---|---|---|---|---|---|---|
| | at.% | | | | | | | | | | | | |
| Z | 75.0 | 0.8 | 22.9 | 1.1 | 0.4 | 0.0 | 0.0 | 0.0 | 0.0 | 0.0 | 0.0 | | |
| FS | 72.0 | 1.9 | 18.5 | 1.5 | | 1.1 | 0.4 | 0.2 | 0.2 | | | 0.6 | 3.6 |
| SSA-PL1 | 69.7 | 1.5 | 3.4 | 0.3 | | 2.5 | 7.7 | 0.6 | 0.7 | 6.2 | | 4.6 | 1.7 |
| CFA | 73.0 | 2.6 | 6.2 | 1.0 | 0.5 | 0.8 | 9.6 | 0.8 | 1.3 | 0.1 | | 0.8 | 3.4 |
| BFA-USA | 73.8 | 1.1 | 7.3 | 1.0 | | 1.2 | 9.6 | 0.7 | 0.6 | | | 0.9 | 3.5 |
| BFA-IT3 | 73.3 | 2.0 | 0.9 | 0.3 | 0.7 | 2.2 | 15.5 | 2.2 | 2.3 | 0.4 | 0.3 | 0.1 | 0.6 |
| BFA-FI1 | 65.8 | 9.6 | 8.4 | 1.0 | | 0.8 | 7.7 | 0.8 | 0.7 | | | 1.0 | 3.9 |
| C-IT2 | 37.2 | 56.6 | 0.3 | | | 1.0 | 3.1 | 0.5 | 0.2 | 0.5 | 0.1 | | 0.3 |
| C-SR | 50.4 | 36.5 | 3.2 | | 4.6 | 0.6 | 0.6 | 3.6 | 0.0 | 0.1 | 0.2 | | 0.3 |
| C-IT1 | 62.8 | 17.3 | 0.1 | 0.1 | 2.5 | 1.2 | 11.1 | 4.1 | 0.1 | 0.5 | 0.1 | | 0.2 |
| BC-UK | 40.0 | 58.1 | 0.1 | 0.2 | | 0.4 | 0.5 | 0.4 | 0.1 | 0.1 | | | 0.2 |
| AC | 38.6 | 48.1 | 3.8 | 0.2 | 6.5 | 0.2 | 0.3 | 0.0 | 0.4 | | 0.0 | 0.3 | 1.7 |
| G | 32.9 | 66.9 | 0.1 | | | | | | | | | | 0.2 |

of the C-SR sample confirms the presence of weakly crystallised quartz (PDF 00–046-1045), similar to the AC sample, and the phase with a structure similar to potassium magnesium aluminosilicate (PDF 04–010-3185). Although the strongest signal at 26.6° (2 theta) also agrees well with graphite (PDF 01–075-2078), the carbon phase is not considered due to the discrepancy between the other measured signals and the carbon phase markers. The CFA and BFA-USA diffractograms are similar and it is possible to identify quartz (PDF 04–008-7651), calcium oxosilicate (PDF 04–011-1393) and calcium-magnesium-iron carbonate (PDF 04–023-8806) in both cases. In addition, several signals can be

attributed to the characterised phases with a structure similar to that of the calcium-sodium silicates (PDF 00–030-1174, 04–023-2764). The patterns of both samples also suggest that the CFA sample contains a higher concentration of quartz (higher intensity of the quartz XRD signals) compared to the BFA-USA sample. Due to the relatively low intensity of the XRD signals compared to the patterns of other samples, it is difficult to make a qualitative analysis of the composition of the BFA-FI1 sample. However, the signals can be attributed to monoclinic silica (PDF 04–012-0809), calcium carbonate (PDF 00–034-0517) and calcium sulphate (01–074-1782). The BFA_IT3 sample contains calcium-rich phases such as: calcium hydroxide (PDF 00–004-0733), calcium carbonate (PDF 00–066-0867), calcium sulphate (PDF 04–011-9876) and calcium phosphate (PDF 04–016-7489). The signal at 26.6° can be defined by either quartz or graphite phase (as in the case of the C-SR sample). However, taking into account the elemental analysis of the sample (Table 2), the signal should be assigned to graphite (PDF 01–075-2078) rather than quartz. The BFA-IT4 sample consists mainly of calcium carbonate (PDF 04–012-6929). Phases such as calcium aluminate (PDF 00–006-0495), sodium phosphates (PDF 00–050-0411, 04–024-3484) and potassium magnesium sulphate (PDF 00–019-0974) can also be attributed to the XRD pattern obtained. The XRD patterns of samples C-IT1 and C-IT2 agree very well with calcium carbonate (PDF 01–089-1304). However, as can be seen, the degree of crystallinity of sample C-IT1 is greater than that of sample C-IT2.

Fig. 3c shows the Raman spectra of the different SWMs and AFs. The structure of the Raman spectra recorded for the samples studied is strongly dependent on the area of the sample surface analysed, so it was necessary to acquire different spots for each sample [30]. The carbon-based samples (G, C-IT1, C-IT2, C-SR, FS, AC, BC-UK) show distinct D and G bands with different peak positions and spectral widths (Fig. 3e). The $I_D/I_G$ ratio was calculated from the normalised intensity of the peak positions. This ratio increases as the material becomes more disordered, with char (C_IT2) at 1.5 and activated carbon (AC) at 1.43 being the most disordered, and graphite (G) at 0.45 being the least disordered [31]. Graphite samples (G) show the D and G bands at 1334 $cm^{-1}$ and 1581 $cm^{-1}$, respectively, with the second order D′ peak at 2700 $cm^{-1}$. The activated carbon (AC) sample shows typical characteristic D and G bands at 1316 $cm^{-1}$ and 1588 $cm^{-1,}$ respectively, and an $I_D/I_G$ ratio of 1.43, indicating a typical disordered structure for activated carbon. The spectrum of the zeolite (Z) sample was dominated by photoluminescence, which effectively covers the entire spectrum, so that almost no specific peaks could be observed. However, weak peaks at 387 $cm^{-1}$ and 478 $cm^{-1}$ can be attributed to mordenite, which is one of the most common and commercially used types of zeolites. Different chars (C-IT1, C-IT2, C-SR, BC-UK) show almost exclusively broad D and G bands with $I_D/I_G$ ratios varying from 1.5 to 0.81. The D peaks are located at 1319 $cm^{-1}$ (C-IT2), 1332 $cm^{-1}$ (C-IT1), 1340 $cm^{-1}$ (C-SR) and 1350 $cm^{-1}$ (BC-UK). The G peak is at 1580–1587 $cm^{-1}$ for all samples with widths ranging from 68 $cm^{-1}$ (C-SR, C-IT2) to 86–90 $cm^{-1}$ (BC-UK, C-IT1). High values of $I_D/I_G$ indicate that these chars are indeed mixed amorphous carbon phases, which can also be deduced from the large widths of the D band ranging from 125 $cm^{-1}$ to 187 $cm^{-1}$. The bands at 226 $cm^{-1}$ and 500 $cm^{-1}$, observed in SSA-PL1 are attributed to the symmetric Fe − O stretching vibration and 291 $cm^{-1}$, 401 $cm^{-1}$, 604 $cm^{-1}$ to a symmetric Fe − O bending vibration, while the broad band observed at 1312 $cm^{-1}$ is associated with two-magnon scattering of hematite [32], typical of Polish wastewater treatment plants due to the use of Fe-based coagulants [33]. The presence of iron in the hematite structure exposed on the surface of fly ashes is one of the promising properties of fly ashes from the point of view of their use as redox catalysts. The fly ash samples (CFA, BFA-USA, BFA-FI1, BFA-IT3) mostly show very similar characteristics. The peaks at 1090 $cm^{-1}$ are indicative of calcium carbonate, which is the most dominant in samples BFA-F1, CFA, BFA-IT3 and BFA-USA, with bands at 290 $cm^{-1}$, 712 $cm^{-1}$ also clearly visible, except for BFA-USA which is covered by another large and broad band at 500–800 $cm^{-1}$, most likely indicative of amorphous oxide glass. Magnifications of the BFA-USA and CFA spectra are shown in Fig. 3d. They show an additional double peak at 836 $cm^{-1}$ and 878 $cm^{-1}$, which we consider to be indicative of the presence of olivine (Mg, Fe)$_2SiO_4$, in particular, its more Mg-rich form, forsterite. The wide band widths should indicate the amorphous and disordered phases, while the shift of the second band is likely to be due to the high temperature exposure calcination of olivine [34] that occurred during the formation of the fly ash. The presence of olivine is possible due to its use in industrial processes such as carbon sequestration during oil combustion. The presence of magnesium carbonate ($MgCO_3$) on olivine is also likely to occur in such processes, generating peaks similar to literature data [35].

### 3.2. Porous hierarchical nanocarbons characterisation

Each porous hierarchical nanocarbons electrode was named with the SWM used and the gas composition during PECVD growth. A representative picture of the top and front views of the synthesized composite (BFA-USA_$H_2$) is reported in Fig. 4a. Fig. 4b shows the micrography of one fibre part of the composite electrodes, in which it is possible to observe a homogeneous dispersion of the SWM within the PAN structure, and the presence of a diffuse open porosity in the range of hundreds of nanometres, resulting from the combined process of phase inversion and plasma etching [24] (Fig. S3). It is important to highlight that by firstly wet-spinning a fibrous composite and secondly casting it into a cylindrical mould, it is possible to maintain the fibre morphology even after the final MPECVD step, with the positive effect of increasing the accessible surface area, compared to casting the polymer blend with SWM directly into the mould. In addition, due to the 1D geometry, shrinkage occurs within the fibre length, reducing the curling that would occur with a 2D geometry. The effect of introducing a carbon precursor ($CH_4$) depends on the SWM type, such as the formation of rod-like shaped clusters on the CFA and BFA-USA spherical particles (Fig. 4d), while no effect is observed with the use of $H_2$-plasma only (Fig. 4c). This could be due to the fact that the carbon in the SWM or in the electrode bulk does not interact in the presence of plasma. A similar result was obtained by Salah et al. when growing CNTs on FA, but using acetylene as precursor [36]. Interestingly, the rod-shaped nanostructure growth is catalysed by metal particles as evidenced by TEM analysis. In particular, Fig. 4f shows typical structures present on the BFA-USA- $CH_4$ sample. They are composed of filaments having inside nanoparticles (dark arrows) and forming intricate skeins. High-resolution (HR) TEM observations have allowed to deeper investigate these structures and to evidence that filaments are formed by the superposition of atomic planes separated by a distance of 0.338 nm compatible with the graphite (002) atomic planes, Fig. 4g. The nanoparticles are also crystalline as revealed by the presence of the atomic planes visible in Fig. 4g (dark arrow) and corresponding to an interplanar distance of 0.597 nm. To better investigate the crystallographic structure of these phases, selected area electron diffraction (SAED) measurements were carried out. Fig. 4h shows the SAED pattern of the sample's area shown in Fig. 4f. Diffraction rings are clearly visible and their corresponding interplanar distances (0.337 nm, 0.203 nm, 0.167 nm and 0.118 nm) can be associated with the (002), (101), (004) and (112) atomic planes of the graphite (PDF 41–1487). In addition to the rings, intense diffraction spots irregularly distributed are present and their interplanar distances correspond to 0.597 nm, 0.278 nm, 0.243 nm, 0.219 nm and 0.135 nm suggesting that nanoparticles are $Fe_2O_3$ (PDF 39–1346). Another recurrent nanostructure formed in different CSWM-composites has a nanowall-like morphology, which is characteristic of $CH_4$-rich precursor in MPECVD synthesis [24]. The HR-TEM image of Fig. 4i shows a typical graphite nanowall-like structure in the BFA-USA- $CH_4$. The evidenced area is magnified in Fig. 4j and the (002) graphite atomic planes are clearly visible. The SWM concentration also affects the electrode morphology, where the formation of dendritic microstructures is a function of the BFA content and it is related to the presence of Mg (Fig. S2). SEM

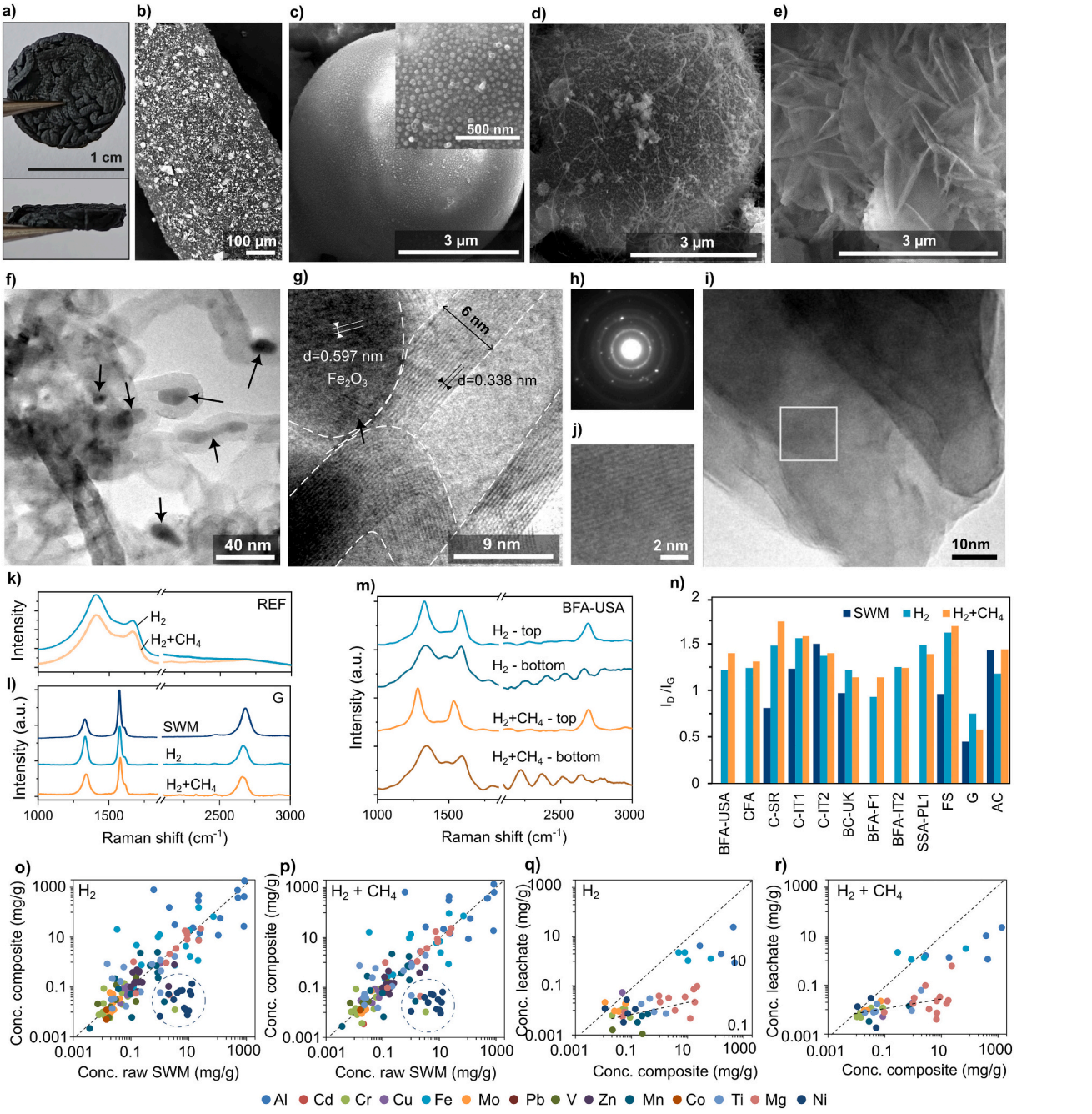


**Fig. 4.** (a) Top and front views of the prepared BFA-USA_$H_2$ sample. (b) BFA-USA_$H_2$ SEM image. SEM image of a spherical particle from (c) BFA-USA_$H_2$ and (d) rod-like nanostructures from BFA-USA-$CH_4$ + $H_2$. (e) SEM image of a nanowall-like graphitic structure from BFA-USA-$CH_4$ + $H_2$. (f,g) TEM and HR-TEM of the rod-like nanostructure and (h) relative SAED pattern. (i,j) HR-TEM of the graphitic nanowall. (k-m) Raman spectra of representative samples (n) with $I_D/I_G$ ratios. (o-p) correlation between the metal concentration found by ICP-OES in the composite electrode sample and the SWM counterpart. (q-r) correlation between the concentration of metals leached into PB during electrochemical test and the concentration found in the bulk counterparts.

micrographs of all electrodes are shown in Fig. S3.

Raman spectra of the reference carbonised PAN sample without any fillers, after the MPECVD process are reported in Fig. 4k. It is possible to notice similar features for both samples, carbonized in the presence of only $H_2$ or $CH_4$ + $H_2$. Composites realised with carbon-rich SWM (such as G) exhibit Raman spectra which are inherited from the SWM (Fig. 4l), while C-poor, such as BFA-USA, show distinct features from the SWM and distinct D and G peaks, characterised by lower $I_D/I_G$ ratio, thus characterised by higher crystallinity (Fig. 4m). The lower degree of disorder could be attributed to the role of calcium oxosilicate and calcium-magnesium-iron carbonate as catalysts for the efficient production of carbon nanostructures [37]. A limitation of the MPECVD growth phase is that both the plasma distribution and the temperature gradient are non-uniform along the depth of the 3D porous PAN scaffolds, resulting in non-uniform growth of carbon nanofeatures and carbonisation. During the fabrication process, the plasma is mostly above the sample, exposing the top side to a much higher energy density than the bottom side of the sample. As a result, the build-up of carbon structures on the top is much enhanced than at the bottom. Immersion of plasma into the samples is limited by high conductivity of samples placed on grounded stage forming a barrier for mostly positively charged ions in the applied $H_2$ and $H_2$ + $CH_4$ gas compositions. The Raman spectra of

the top-bottom comparison in Fig. 4m exhibit that the top of the sample reveals more ordered forms, while the bottom of the sample results in high content of defects, as confirmed by the presence of D and G bands of larger width in the spectra of the sample's bottom. In addition, the spectra of the top side are dominated by the newly grown structures with minor or no remnants of the precursor powders, whereas the spectra of the bottom side are more similar to the precursor powders, implying that much less effective growth of carbonaceous structures has occurred on this side of the sample. For comparison, all the Raman spectra are reported in Fig. S4.

Results of the ICP analysis are reported in Table S3. The most abundant elements in most of the SWMs samples are Al, Fe, Mg, and Ti, while Cu, Cr, Mo, Ni, V, Zn, Co and Mn have been found in specific samples. Au has been found in one sample, as well as Cd. Fig. 4o,p show that the CCVD processes ($H_2$ or $H_2 + CH_4$) do not affect the final content of metals within the PAN-based composite, except of Ni, for which a 100-fold lower concentration is found. In particular, this behaviour occurs both under $H_2$ and $CH_4$ conditions, suggesting the role of $H_2$ plasma in forming complexes with other components in the composite during digestion, making it less available for analysis. A few of the metals have been found leaching into the aqueous sample. Al and Fe were found in considerable amounts, and Cr, Mo, Mn, Ti, Mg were found in almost all the water samples, but in lower quantities. Cu, Ni, V were found only in a few samples, despite being present in most of the SWMs. No difference in leaching behaviour between the $H_2$ and $H_2$ + CH4 processes was found (Fig. 4q,r).

Water vapour adsorption isotherm enables to provide valuable information about the adsorption behaviour of a material, such as its surface area, pore size distribution, and adsorption capacity. Only the raw PAN composite, without any SWM, is represented by a type I isotherm (Fig. S5), which has a concave shape with respect to the $p/p_0$ axis, with the adsorption capacity gradually approaching a maximum value. This maximum uptake is determined by the volume of accessible micropores rather than the internal surface area, suggesting the presence of a pore size distribution over a wider range of micropores and narrow mesopores [27]. On the other hand, sigmoidal isotherms such as type IV and type V are commonly observed in water vapour adsorption on porous materials due to capillary condensation in pores. In fact, the type IV isotherm is typical of mesoporous materials that have moderate surface areas and pore sizes. Adsorption occurs by capillary condensation in the mesopores and is reversible. On the other hand, materials characterised by the type V isotherm generally have narrow micropores or ultramicropores with high surface areas and small pore sizes. Adsorption occurs by multi-layer adsorption of water molecules in the micropores. As we have seen, the MPECVD process on the SWM composites induces changes in the morphology of the composites, which are reflected in changes in the isotherms, including the maximum adsorption capacity ($Q_{max}$), K, m and C. Taking into account the $Q_{max}$, three different behaviours can be distinguished:

- A decrease in the final adsorption capacity of the composite compared to the raw SWM. Water vapour adsorption on AC has a

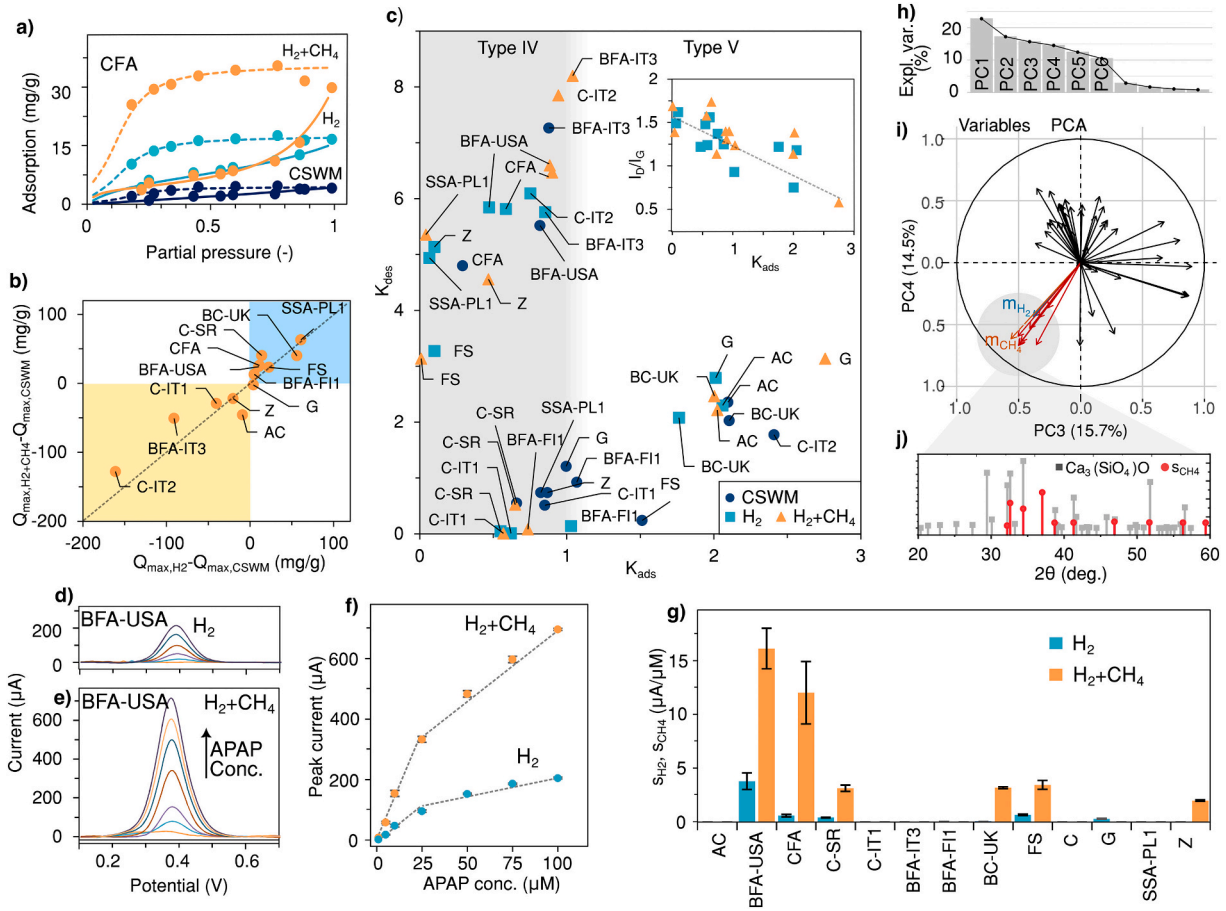


**Fig. 5.** (a) Typical water adsorption isotherm for the CFA sample. Plot of (b) the net gain in terms of $Q_{max}$ for both $H_2$ and $H_2$ + $CH_4$ processes, (c) correlations between $K_{ads}$ and $K_{des}$ and its dependence on the $I_D/I_G$ Raman ratio. APAP detection by DPV by (d) $H_2$ and (e) $CH_4$ sample and (f) their correlation with APAP concentration for a representative sample (BFA-USA) and the (g) sensitivity ($s_{H2}$, $s_{CH4}$) of all the synthesized electrodes. (h) Scree plot of the PCA performed on the XRD dataset and (i) projection of $s_{H2}$, $s_{CH4}$ in the space defined by PC3 and PC4. The variables in red have been plotted in (j) and their height is the Euclidean distance to $s_{CH4}$.

type V isotherm in the IUPAC classification. AC is a technical adsorbent material characterised by a large surface area and accessible diffuse microporosity; its incorporation into the polymer matrix and subsequent treatment by MPECVD results in a deterioration of the final adsorption capacity, probably due to the partial clogging of the pores by the overgrown carbon layer. This group also includes C-IT2, BFA-IT3 (Fig. 5-d, highlighted in yellow).

- The absence of changes in $Q_{max}$. This is the case for sample G, where the final capacity is slightly changed, while the $H_2$ and $CH_4$+$H_2$ isotherms are similar to the raw one, suggesting that limited growth process took place, as also previously shown by the Raman spectra.
- An increase in the final adsorption capacity of the composite (Fig. 5b, highlighted in light blue). Within this group, two subgroups can be identified:
  - the formation of a large hysteresis during desorption, as in the case of CFA (Fig. 5a), BFA-USA, BFA-FI1;
  - preservation of the same isotherm type, such as FS, C-SR, BC-UK and SSA-PL1.

The absolute difference in $Q_{max}$ between the SWM and the composite after MPECVD is shown in Fig. 5b. Firstly, the quasi-linear relationship suggests that the $H_2$ plasma atmosphere (present in both MPECVD growth conditions) is the main parameter affecting $Q_{max}$. Secondly, almost all samples, except AC, are characterised by higher $Q_{max}$ during $CH_4$-assisted growth, suggesting that the formation of additional carbon structures and functional groups is beneficial for adsorption. Indeed, from the selected micrographs in Fig. S6, representing the classes mentioned above, it is possible to observe that the surface morphology may play a predominant role. According to Buttersack [26], type IV and type V isotherms can be distinguished by the C parameter. We have found that such a distinction is better represented by the K parameter; indeed, the type V isotherm is given for $K > 1$. Moreover, by plotting $K_{ads}$ against $K_{des}$, two linear trends are observed: the first with slope $m = 1$, indicating capillary condensation at the same partial pressure, and the second for $m = 4$, highlighting the presence of a larger hysteresis. Moreover, since K is related to capillary condensation, plotting it against the characteristic Raman $I_D/I_G$ ratio, reveals an indirect correlation (Fig. 5c, inset). Indeed, higher disorder (higher $I_D/I_G$ ratio) could be associated with increased porosity and surface area, providing more adsorption sites for water vapour during capillary condensation. In addition, the presence of defects and functional groups on the surface of the carbon nanomaterial could also alter the surface chemistry of the material, affecting capillary condensation.

### 3.3. Porous hierarchical nanocarbons as electrodes

Examples of APAP oxidation by DPV are shown in Fig. 5d,e for the $H_2$ and $H_2$ + $CH_4$ BFA-USA composites, respectively. It is possible to observe an oxidation peak at about 0.36 V vs. AgCl, lower than those (0.38–0.48 V) found in similar composites prepared by MPECVD without the addition of fillers [24]. The relationship between APAP concentration and the oxidation current peak in DPV follows two linear trends for lower and higher concentrations, where as the concentration of APAP increases, the oxidation current peak also increases linearly (Fig. 5f). The slope of the linear correlation (indicating the sensitivity of the method to APAP) was specified as $s_{H2}$ and $s_{CH4}$ for the two composite electrodes and plotted in Fig. 5g. All $H_2$ + $CH_4$ composites show a much higher sensitivity than the corresponding $H_2$-treated counterparts.

The raw CFA and BFA SWMs are very similar when both Raman and XRD analyses are compared. Interestingly, the carbon content of both raw powders is the lowest among SWM and AF (1.1 and 2.6%, respectively) (Fig. 3b,d and Table 2). However, their relative composites show the highest sensitivity to APAP oxidation. Moreover, the composite synthesized in the presence of $CH_4$ exhibited a current 3 times higher than that with $H_2$ alone, which can be attributed to the CVD growth nanostructure and is catalysed by the specific SWMs. As highlighted by the Raman spectra, the presence of forsterite, a Mg end-member of olivine, may be responsible for the growth of amorphous carbon on the SWM surface [38]. SEM micrographs show that the carbon fibres are also formed on the iron-rich cenospheres, which, due to their high silica content, are known to act as catalysts or catalytic supports for the esterification reaction [39]. Indeed, the presence of iron oxide on the surface of cenospheres is known to be effective for the deep oxidation of methane [40], which would explain the enhanced carbon growth. However, it remains to be explained why composite samples derived from BFA-FI1, although also rich in cenospheres (Fig. 2g, Fig. 3a,), are not electroactive. To better understand the possible presence of a specific catalyst explaining the enhanced electrochemical activity, the SWM XRD dataset was analysed by PCA to identify which peaks are due to electroactive behaviour. SWM peak positions and intensities were extracted from the diffractograms and used as active variables on which PCA was performed. The first 6 variables explained 93.0% of the total variance (Fig. 5h) and, by providing $s_{H2}$ and $s_{CH4}$ as additional quantitative variables, were the most highly expressed in PC3 and PC4. The Euclidean distances between $s_{CH4}$ and all other variables in the PC3-PC4 projection were calculated (Fig. S7) and the top ten (Fig. 5i, grey circle) were selected. As each variable is related to a specific peak position, the resulting "pseudo-reference" is plotted in red in Fig. 5j, where the height is the previously calculated distance. It is possible to observe that the reference (PDF 04–011-1393), $Ca_3(SiO_4)O$, overlaps and shares the strongest features, supporting the hypothesis that it may act as a catalyst during the MPECVD process. On the other hand, wollastonite is a type of calcium inosilicate ($CaSiO_3$) material that has been shown to support and catalyse the growth of aligned CNTs with a purity of 98.7% [41]. However, the presence of an inorganic catalyst is not the only reason for obtaining an electrochemically active composite. In fact, the presence of highly disordered carbon, containing a large number of edges and defects, makes it an ideal platform for catalysing the growth of carbon nanomaterials. C-SR, BC-UK and the fine fraction of FS have an $I_D/I_G$ ratio slightly below 1 and are electroactive towards APAP. Interestingly, no correlation was found between the metal concentrations in the SWM (Table S4) and the composite electroactivity (expressed as APAP sensitivity), highlighting that the presence of metals in the bulk is not a necessary condition for the catalytic growth of carbon nanostructures.

## 4. Conclusion

In conclusion, the incorporation of SWM into porous hierarchical nanocarbons composites has been shown to have several significant microstructural and physicochemical effects. The presence of SWM reduces fibre shrinkage during fibre stabilisation, providing potential benefits for practical applications. In addition, the ability of the composites to oxidise APAP varies with growth conditions, with samples grown in the presence of $CH_4$ + $H_2$ exhibiting higher current densities than their $H_2$ counterparts. The catalytic role of SWM in carbon growth is not universal and two pathways have been suggested. For samples with low carbon content, specific inorganic compounds, such as calcium oxosilicate and iron oxides, are found to catalyse carbon growth. On the other hand, carbon-rich samples show an optimum $I_D/I_G$ ratio of about 0.9, where defects and active sites provide favourable forms for nucleation and secondary carbon growth. Interestingly, the presence of metals known as catalysts, such as Fe and Ni, does not directly correlate with the composite electroactivity for APAP oxidation. Furthermore, the leaching of heavy metals from the composites into solutions is of minimal concern due to the very low concentrations found. The modification of the composites after the chemical vapour deposition process is well described by water vapour adsorption isotherms, revealing the formation of mesopores in some composites, demonstrated by large hysteresis during desorption. By using waste materials as catalysts, this research aligns seamlessly with the principles of the circular economy, which promotes the reuse of discarded materials to reduce environmental impact and dependence on virgin resources. This approach paves the

way for sustainable and environmentally friendly practices in carbon nanomaterial synthesis, with a particular focus on the electrochemical oxidation of pharmaceuticals.

## CRediT authorship contribution statement

**Maciej J. Głowacki:** Formal analysis, Methodology, Investigation, Validation, Writing – original draft. **Katarzyna Karpienko:** Formal analysis, Methodology, Investigation, Writing – original draft. **Maciej S. Wróbel:** Formal analysis, Validation, Investigation. **Karol Szczodrowski:** Formal analysis, Investigation, Resources, Writing – original draft. **Chiara Giosuè:** Formal analysis, Resources, Writing – original draft. **Gianni Barucca:** Methodology, Formal analysis, Investigation, Resources. **Maria Letizia Ruello:** Methodology, Resources, Writing – review & editing. **Robert Bogdanowicz:** Methodology, Resources, Funding acquisition, Writing – review & editing, Supervision. **Mattia Pierpaoli:** Conceptualization, Methodology, Formal analysis, Investigation, Resources, Funding acquisition, Project administration, Supervision, Visualization.

## Declaration of competing interest

None.

## Data availability

Data is available at https://doi.org/10.34808/ynj6-6r28 under CC BY 4.0 license.

## Acknowledgements

Funding from the National Science Centre, Poland, under the agreement 2022/45/B/ST8/02847 is acknowledged (M.P.), as well as CI TASK and DS funds of the Faculty of Electronics, Telecommunications, and Informatics, Gdańsk University of Technology (M. W.).

## Appendix A. Supplementary data

Supplementary data to this article can be found online at https://doi.org/10.1016/j.susmat.2024.e00933.

## References

[1] L. Deng, W. Guo, H.H. Ngo, X. Zhang, D. Wei, Q. Wei, S. Deng, Novel catalysts in catalytic upcycling of common polymer wastes, Chem. Eng. J. 471 (2023) 144350, https://doi.org/10.1016/j.cej.2023.144350.
[2] S. De Gisi, G. Lofrano, M. Grassi, M. Notarnicola, Characteristics and adsorption capacities of low-cost sorbents for wastewater treatment: a review, Sustain. Mater. Technol. 9 (2016) 10–40, https://doi.org/10.1016/j.susmat.2016.06.002.
[3] O. Guselnikova, O. Semyonov, E. Sviridova, R. Gulyaev, A. Gorbunova, D. Kogolev, A. Trelin, Y. Yamauchi, R. Boukherroub, P. Postnikov, "Functional upcycling" of polymer waste towards the design of new materials, Chem. Soc. Rev. 52 (2023) 4755–4832, https://doi.org/10.1039/d2cs00689h.
[4] O. Vieira, R.S. Ribeiro, J.L. Diaz de Tuesta, H.T. Gomes, A.M.T. Silva, A systematic literature review on the conversion of plastic wastes into valuable 2D graphene-based materials, Chem. Eng. J. 428 (2022), https://doi.org/10.1016/j.cej.2021.131399.
[5] A. Bazargan, G. McKay, A review - synthesis of carbon nanotubes from plastic wastes, Chem. Eng. J. 195–196 (2012) 377–391, https://doi.org/10.1016/j.cej.2012.03.077.
[6] V. Jourdain, C. Bichara, Current understanding of the growth of carbon nanotubes in catalytic chemical vapour deposition, Carbon N. Y. 58 (2013) 2–39, https://doi.org/10.1016/j.carbon.2013.02.046.
[7] G.P. Gakis, S. Termine, A.F.A. Trompeta, I.G. Aviziotis, C.A. Charitidis, Unraveling the mechanisms of carbon nanotube growth by chemical vapor deposition, Chem. Eng. J. 445 (2022) 136807, https://doi.org/10.1016/j.cej.2022.136807.
[8] S. Nishimura, A. Takagaki, K. Ebitani, Characterization, synthesis and catalysis of hydrotalcite-related materials for highly efficient materials transformations, Green Chem. 15 (2013) 2026–2042, https://doi.org/10.1039/c3gc40405f.
[9] H.U. Modekwe, M.A. Mamo, M.O. Daramola, K. Moothi, Catalytic performance of calcium titanate for catalytic decomposition of waste polypropylene to carbon nanotubes in a single-stage CVD reactor, Catalysts 10 (2020) 1–20, https://doi.org/10.3390/catal10091030.
[10] F. Dziike, P.J. Franklyn, L. Hlekelele, S. Durbach, Recovery of waste gold for the synthesis of gold nanoparticles supported on radially aligned nanorutile: the growth of carbon nanomaterials, RSC Adv. 10 (2020) 28090–28099, https://doi.org/10.1039/d0ra03797d.
[11] F. Li, C. Zhou, P. Yang, B. Wang, J. Hu, J. Wei, Q. Yu, Direct synthesis of carbon nanotubes on fly ash particles to produce carbon nanotubes/fly ash composites, Front. Struct. Civ. Eng. 13 (2019) 1405–1414, https://doi.org/10.1007/s11709-019-0564-0.
[12] K.M. Rambau, N.M. Musyoka, N. Manyala, J. Ren, H.W. Langmi, M.K. Mathe, Preparation of carbon nanofibers/tubes using waste tyres pyrolysis oil and coal fly ash derived catalyst, J. Environ. Sci. Heal. Part A Toxic/Hazardous Subst. Environ. Eng. 53 (2018) 1115–1122, https://doi.org/10.1080/10934529.2018.1474594.
[13] X. Zhang, J. Li, B. He, S. Yang, Y. Li, D. Chen, Y. Li, Y. Peng, Phase transformation and carbon precipitation of coal fly ash magnetospheres during a CVD process for microwave adsorption, Ceram. Int. 45 (2019) 18980–18987, https://doi.org/10.1016/j.ceramint.2019.06.138.
[14] M. Pierpaoli, M. Rycewicz, A. Łuczkiewicz, S. Fudala-Książek, R. Bogdanowicz, M. L.M.L. Ruello, S. Fudala-Ksią Zek, R. Bogdanowicz, M.L.M.L. Ruello, Electrodes criticality: the impact of CRMs in the leachate electrochemical oxidation, Manuf. Rev. 7 (2020) 7, https://doi.org/10.1051/mfreview/2020006.
[15] Y. Jin, J. Ren, J. Chen, Z. Dai, B. Li, X. Zhou, Controllable preparation of helical carbon nanofibers by CCVD method and their characterization, Mater. Res. Express. 5 (2018), https://doi.org/10.1088/2053-1591/aaa09c.
[16] D.C.D. Nath, V. Sahajwalla, Application of fly ash as a catalyst for synthesis of carbon nanotube ribbons, J. Hazard. Mater. 192 (2011) 691–697, https://doi.org/10.1016/j.jhazmat.2011.05.072.
[17] D. Farhanian, C.A. Dorval Dion, W. Raphael, G. De Crescenzo, J.R. Tavares, Combined extraction and functionalization of low-cost nanoparticles from municipal solid waste fly ash through PICVD, J. Environ. Chem. Eng. 2 (2014) 2242–2251, https://doi.org/10.1016/j.jece.2014.09.019.
[18] J.E. Park, H.K. Youn, S.T. Yang, W.S. Ahn, CO2 capture and MWCNTs synthesis using mesoporous silica and zeolite 13X collectively prepared from bottom ash, Catal. Today 190 (2012) 15–22, https://doi.org/10.1016/j.cattod.2011.09.032.
[19] J. Zhang, A. Tahmasebi, J.E. Omoriyekomwan, J. Yu, Production of carbon nanotubes on bio-char at low temperature via microwave-assisted CVD using Ni catalyst, Diamond Relat. Mater. 91 (2019) 98–106, https://doi.org/10.1016/j.diamond.2018.11.012.
[20] D.R. Paul, W.J. Koros, R.Y.F. Liu, Y.S. Hu, E. Baer, A. Hiltner, H.D. Keith, R.Y. F. Liu, A. Hiltner, E. Baer, R.E. Cohen, A. Bellare, R.J. Albalak, W. Hu, G. Reiter, Nitrogen-Doped Carbon Nanotube 323, 2009.
[21] S.V. Sawant, A.W. Patwardhan, J.B. Joshi, K. Dasgupta, Boron doped carbon nanotubes: synthesis, characterization and emerging applications – a review, Chem. Eng. J. 427 (2022) 131616, https://doi.org/10.1016/j.cej.2021.131616.
[22] M. Pierpaoli, M. Szopińska, A. Olejnik, J. Ryl, S. Fudala-Ksiażek, A. Łuczkiewicz, R. Bogdanowicz, Engineering boron and nitrogen codoped carbon nanoarchitectures to tailor molecularly imprinted polymers for PFOS determination, J. Hazard. Mater. 458 (2023), https://doi.org/10.1016/j.jhazmat.2023.131873.
[23] M. Pierpaoli, M. Ficek, P. Jakobczyk, J. Karczewski, R. Bogdanowicz, Self-assembly of vertically oriented graphene nanostructures: multivariate characterisation by Minkowski functionals and fractal geometry, Acta Mater. (2021) 116989, https://doi.org/10.1016/j.actamat.2021.116989.
[24] M. Pierpaoli, P. Jakóbczyk, B. Dec, C. Giosuè, N. Czerwińska, A. Lewkowicz, M. L. Ruello, R. Bogdanowicz, A novel hierarchically-porous diamondized polyacrylonitrile sponge-like electrodes for acetaminophen electrochemical detection, Electrochim. Acta 430 (2022) 1–11, https://doi.org/10.1016/j.electacta.2022.141083.
[25] I.M. Klotz, F.M. Walker, R.B. Pivan, The binding of organic ions by proteins, J. Am. Chem. Soc. 68 (1946) 1486–1490, https://doi.org/10.1021/ja01212a030.
[26] C. Buttersack, Modeling of type IV and v sigmoidal adsorption isotherms, Phys. Chem. Chem. Phys. 21 (2019) 5614–5626, https://doi.org/10.1039/c8cp07751g.
[27] M. Thommes, K. Kaneko, A.V. Neimark, J.P. Olivier, F. Rodriguez-Reinoso, J. Rouquerol, K.S.W. Sing, Physisorption of gases, with special reference to the evaluation of surface area and pore size distribution (IUPAC technical report), Pure Appl. Chem. 87 (2015) 1051–1069, https://doi.org/10.1515/pac-2014-1117.
[28] O.M. Sharonova, N.N. Anshits, M.A. Fedorchak, A.M. Zhizhaev, A.G. Anshits, Characterization of Ferrospheres recovered from high-calcium Fly ash, Energy Fuels 29 (2015) 5404–5414, https://doi.org/10.1021/acs.energyfuels.5b01618.
[29] E. Haustein, A. Kuryłowicz-Cudowska, A. Łuczkiewicz, S. Fudala-Książek, B. M. Cieślik, Influence of cement replacement with sewage sludge ash (SSA) on the heat of hydration of cement mortar, Materials (Basel). 15 (2022), https://doi.org/10.3390/ma15041547.
[30] P. Rybowicz, M. Mochnaczewski, M. Kozieł, Ł. Uruski, A. Łagosz, M. Michalik, L. Chmielarz, A. Adamski, Key parameters of Fly ashes generated from the industrial energy sector decisive for their pro-ecological applications, Energy and Fuels. 34 (2020) 6229–6238, https://doi.org/10.1021/acs.energyfuels.9b04426.
[31] D.B. Schuepfer, F. Badaczewski, J.M. Guerra-Castro, D.M. Hofmann, C. Heiliger, B. Smarsly, P.J. Klar, Assessing the structural properties of graphitic and non-graphitic carbons by Raman spectroscopy, Carbon N. Y. 161 (2020) 359–372, https://doi.org/10.1016/j.carbon.2019.12.094.
[32] Y. Yin, J. Yin, W. Zhang, H. Tian, Z. Hu, M. Ruan, H. Xu, L. Liu, X. Yan, D. Chen, FT-IR and micro-Raman spectroscopic characterization of minerals in high-calcium coal ashes, J. Energy Inst. 91 (2018) 389–396, https://doi.org/10.1016/j.joei.2017.02.003.

[33] M. Smol, C. Adam, S.A. Kugler, Thermochemical treatment of sewage sludge ash (SSA)-potential and perspective in Poland, Energies 13 (2020) 1–17, https://doi.org/10.3390/en13205461.
[34] R. Michel, M.R. Ammar, J. Poirier, P. Simon, Phase transformation characterization of olivine subjected to high temperature in air, Ceram. Int. 39 (2013) 5287–5294, https://doi.org/10.1016/j.ceramint.2012.12.031.
[35] M.H. Fasihnikoutalab, A. Asadi, B.K. Huat, P. Westgate, R.J. Ball, S. Pourakbar, Laboratory-scale model of carbon dioxide deposition for soil stabilisation, J. Rock Mech. Geotech. Eng. 8 (2016) 178–186.
[36] N. Hintsho, A. Shaikjee, P.K. Triphati, H. Masenda, D. Naidoo, P. Franklyn, S. Durbach, Effect of nitrogen and hydrogen gases on the synthesis of carbon nanomaterials from coal waste fly ash as a catalyst, J. Nanosci. Nanotechnol. 16 (2016) 4672–4683, https://doi.org/10.1166/jnn.2016.12434.
[37] J. Zhu, J. Jia, F.L. Kwong, D.H.L. Ng, S.C. Tjong, Synthesis of multiwalled carbon nanotubes from bamboo charcoal and the roles of minerals on their growth, Biomass Bioenergy 36 (2012) 12–19, https://doi.org/10.1016/j.biombioe.2011.08.023.
[38] S. Kawasaki, M. Shinoda, T. Shimada, F. Okino, H. Touhara, Single-walled carbon nanotubes grown on natural minerals, Carbon N. Y. 44 (2006) 2139–2141, https://doi.org/10.1016/j.carbon.2006.03.015.
[39] V.S. Chandane, A.P. Rathod, K.L. Wasewar, S.S. Sonawane, Efficient cenosphere supported catalyst for the esterification of n-octanol with acetic acid, Comptes Rendus Chim. 20 (2017) 818–826, https://doi.org/10.1016/j.crci.2017.03.007.
[40] S.N. Vereshchagin, N.N. Anshits, A.N. Salanov, O.M. Sharonova, T. A. Vereshchagina, Microspheres of fly ash as a source for catalytic supports, adsorbents and catalysts, Chem. Sustain. Dev. 11 (2003) 303–308.
[41] M.Q. Zhao, Q. Zhang, J.Q. Huang, J.Q. Nie, F. Wei, Advanced materials from natural materials: synthesis of aligned carbon nanotubes on wollastonites, ChemSusChem 3 (2010) 453–459, https://doi.org/10.1002/cssc.201000002.